Journal of Power Sources 584 (2023) 233539

Contents lists available at ScienceDirect

Journal of Power Sources

journal homepage: www.elsevier.com/locate/jpowsour

Image-based pore-scale modelling of the effect of wettability on breakthrough capillary pressure in gas diffusion layers

Min Li [a,b], Sajjad Foroughi [a,*], Jiafei Zhao [b], Branko Bijeljic [a], Martin J. Blunt [a]

[a] Department of Earth Science and Engineering, Imperial College London, SW7 2BP, London, United Kingdom
[b] Key Laboratory of Ocean Energy Utilization and Energy Conservation of the Ministry of Education, Dalian University of Technology, Dalian, 116024, China

HIGHLIGHTS

- Pore network modelling is extended to study fibrous materials.
- The model estimates water breakthrough pressure accurately.
- The model is extended to study primary imbibition and drainage in mixed-wet media.
- A representative wettability can be determined to match experiment.

ARTICLE INFO

Keywords:
Gas diffusion layers
Pore network model
Breakthrough capillary pressure
Mixed wettability
Pore occupancy

ABSTRACT

Wettability design is of crucial importance for the optimization of multiphase flow behaviour in gas diffusion layers (GDLs) in fuel cells. The accumulation of electrochemically-generated water in the GDLs will impact fuel cell performance. Hence, it is necessary to understand multiphase displacement to design optimal pore structures and wettability to allow the rapid flow of gases and water in GDLs over a wide saturation range. This work uses high-resolution *in situ* three-dimensional X-ray imaging combined with a pore network model to investigate the breakthrough capillary pressure and water saturation in GDLs manufactured with different mass fractions of polytetrafluoroethylene coating: 5, 20, 40, and 60%, making them more hydrophobic. We first demonstrate that the pore network extraction method provides representative networks for the fibrous porous media examined. Then, using a pore-network flow model we simulate water invasion into initially gas-filled fibrous media, and analyze the effect of wettability on breakthrough capillary pressure and water saturation. With an appropriate pore-scale characterization of wettability, a pore network model can match experimental results and predict displacement behaviour.

1. Introduction

Polymer electrolyte fuel cells (PEFCs) are efficient clean energy-conversion devices consisting of a polymer electrolyte membrane (PEM), catalyst layers (CLs), microporous layers (MPLs), gas diffusion layers (GDLs), bipolar plates, current collectors and an end plate [1,2]. Water is produced in the cathode catalyst layers through the electrochemical reaction between hydrogen and oxygen [3]. Water clusters can intrude into the MPLs and GDLs [4], and excessive water accumulation will lead to water flooding [5], clogging the pore space and preventing gas flow to the CLs. This will result in the limitation of oxygen mass transport and inhibit oxygen movement to the reaction interface of CLs [6], interfering with the electrochemical process. Therefore, understanding the fundamentals of the water transport process in GDLs is critical to improving water removal, which plays a key role in water management and optimizing the performance of fuel cells [7].

It has been demonstrated that water transport in GDLs is dominated by capillary pressure (gas pressure minus the water pressure), which is controlled by pore structure (geometry and topology) and wettability [6, 8–12]. The commonest GDLs, consisting of carbon paper or carbon cloth with complex microporous materials and hydrophilic and hydrophobic carbon fibres [13], can be designed to have a specific wettability using methods such as solvent-based coating [14], electrospinning [15], and plasma treatment [16]. Polytetrafluoroethylene (PTFE), which both binds the fibres and changes the surface wettability, offers a relatively simple and straightforward method for creating mixed wettability (that

* Corresponding author.
E-mail address: s.foroughi@imperial.ac.uk (S. Foroughi).

https://doi.org/10.1016/j.jpowsour.2023.233539
Received 29 April 2023; Received in revised form 14 July 2023; Accepted 19 August 2023
Available online 14 September 2023

is the fibres present a mix of uncoated, hydrophilic, surfaces and coated, hydrophobic, surfaces) [14,17]. The PTFE coating adheres to the surface of carbon fibres, and fills or blocks the pore space of the GDLs decreasing its porosity as well as changing the wettability [14,18]. Ideally the pore structure and wettability should be designed to optimize water removal and oxygen transport [9,19–21].

Water generation and accumulation at the membrane/catalyst interface lead to a build up of water pressure [13]. The minimum pressure required for water to cross GDLs to the bipolar plate is termed the breakthrough capillary pressure [10,22–24]. Generally, the breakthrough capillary pressure in hydrophobic GDLs with a high PTFE content is larger in magnitude (more negative) than for hydrophilic samples [23]. Santamaria et al. [22] and Shojaei et al. [25] measured the breakthrough capillary pressure in a mixed-wet GDL with PTFE coating and found values ranging between −3 and −6 kPa. However, some experimental observations provided evidence that adding more PTFE to the carbon fibre surface of GDLs results in little change in the breakthrough capillary pressure, even though the material becomes more hydrophobic [13,26]. There is a delicate balance between breakthrough capillary pressure and water removal that needs to be revealed to guide how to improve the ability of water removal in GDLs.

To complement experimental measurements different numerical methods have been developed to study multiphase flow in GDLs, including the volume of fluid (VOF) approach [27–31], the lattice Boltzmann method (LBM) [19,32,33], and pore network models (PNMs) [6,9,34]. Niu et al. [27] used a VOF model to predict the relationship between capillary pressure and water saturation in GDLs considering different spatial wettability distributions. Moreover, Niu et al. [28] showed that the flow of water droplets can be hindered in GDLs due to capillary effects at higher hydrophobicity. Water preferentially flows through the connected hydrophilic network and facilitates water removal from GDLs [6,19]. Comparing different numerical methods, PNMs are computationally faster than LBM and VOF but do need to be based on a realistic pore-space geometry.

X-ray microtomography is a non-destructive imaging technique to study multiphase flow in porous media [35,36], in applications such as petroleum engineering [35], soil and groundwater [37], CO_2 storage [38], hydrogen storage [39,40], and water and gas flow in fuel cells [25,41]. In recent years, this technique was used to observe the interior structure of three-dimensional (3D) fibrous media and provide insight into the wettability distribution [25,42] and interfacial curvature [25]. We utilize X-ray images of GDLs to quantify the pore network topology and to compare the measured fluid configuration with that predicted by PNMs.

In this work, we employ high-resolution *in situ* three-dimensional X-ray imaging combined with PNM to investigate water transport in mixed wettability GDLs manufactured with different mass fractions of PTFE: 5, 20, 40, and 60%. Our primary focus is to elucidate the influence of contact angle and pore structure on the breakthrough capillary pressure and water saturation. Initially, we extract pore networks of the fibrous media and then simulate flow for mixed wettability conditions. Next, we present an analysis of the sensitivity of the breakthrough capillary pressure and water saturation to contact angle, and compare the model predictions with the experimental data. Finally, we quantify pore occupancy for the experiment and model to reveal the impact of pore size on displacement and fluid distribution.

2. Materials and methods

2.1. Experiment procedure

To analyze the water breakthrough in GDLs using micro-CT experiments, Shojaei et al. [25] performed four tests using samples coated with 5, 20, 40, and 60% PTFE (AvCarb MGL 370 Carbon Paper). The coating percentage refers to the mass fraction of PTFE in the material and not the fraction of the solid surface coated with the plastic. The porosities were 0.68 ± 0.01, 0.67 ± 0.01, 0.69 ± 0.03, and 0.37 ± 0.03 respectively. These porosity values were determined from the segmented dry images and the uncertainty measurements were obtained from thresholding and machine learning-based trainable Weka segmentation (TWS) methods. Note that only for the 60% PTFE case do we see a significant drop in porosity.

All samples were scanned using a Zeiss Versa XRM-510 X-ray micro-CT scanner with a voxel size of 2.05 μm. Reconstruction of all 3D tomogram datasets was performed using the Zeiss Reconstructor software to generate high-quality 3D images. Micro-CT imaging was conducted to scan the dry samples first. Then, air in the samples was displaced by a brine solution made from deionized water with 15 wt% potassium iodide. This brine was injected at a rate of 7 μL/h until water breakthrough occurred in the vertically aligned GDLs. The experiments were continued for 30 min before shutting off the pump, and the wet samples were scanned. The breakthrough capillary pressure was determined by measuring the maximum pressure during water injection into GDLs. The breakthrough water saturation measurements were obtained from segmented wet image samples. In addition, the distribution of contact angle was measured directly on the images using an automated

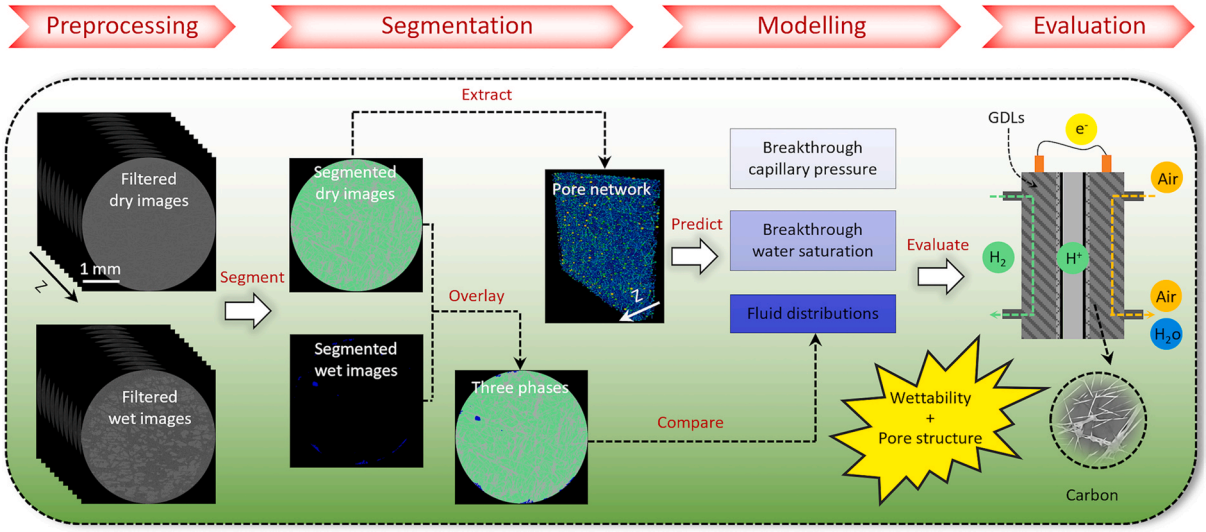

Fig. 1. The workflow for prediction and evaluation of multiphase flow in GDLs considering X-ray images of fibrous structures and coating that rendered them mixed-wet. Breakthrough capillary pressure and water saturation are compared from the experiment and image-based PNM simulation.

method [43]. A more comprehensive description of the experiment workflow can be found in Shojaei et al. [25].

Once the X-ray images of GDLs with air/water distributions are available, the workflow that includes preprocessing, segmentation, modelling and evaluation can be applied, as depicted in Fig. 1.

2.2. Imaging methods and processing

The wet images were registered with the dry images using commercial image analysis software, Avizo 9.3 (ThermoFisher Scientific) to ensure accurate alignment. Dry and wet images were processed using a 3D non-local filter to reduce noise, as shown in Fig. 2. The filtered dry images were segmented into two classes (air and fibres) using the machine learning TWS plugin in Fiji software [44]. The plugin is trained using manual annotations of the training images, which are used to generate features that are used to perform the segmentation, resulting in a more accurate segmentation compared to traditional methods. However, TWS requires extensive computational resources, including CPU and memory, to execute the segmentation task. Filtered wet images were segmented into two classes (air + fibres and water) through interactive thresholding segmentation, where user-defined threshold values were used to segment classes according to intensity values. Finally, the segmented wet images were overlayed on the segmented dry images to obtain three different phases (water, air and fibre), as shown in Fig. 2.

2.3. Pore network modelling

To simulate multiphase flow through GDLs, the first step is to extract the pore network structure from the dry image. For this purpose, we employed the maximal ball pore network extraction code [45,46]. This algorithm computes the distance map – the distance from any point in the void space to the nearest solid – to identify pores and throats. The local maxima in the distance map define pores, and the radius of the pores is represented by the maximum inscribed sphere. The constrictions between the adjacent pores define throats. More details about the algorithm can be found in Dong and Blunt and Raeini et al. [45,46]. The pore or throat is described by a shape factor G, which is defined as [47]:

$$G = \frac{R^2}{4A} \tag{1}$$

where G is the pore or throat shape factor, R is the inscribed radius. A is the cross-sectional area of the pore or throat.

After extracting the network from the images, the pore-network flow model [48] was modified to predict water and gas flow through GDLs. The water invades the pores and throats of the network, which is initially completely saturated with air. This process is primary invasion which may be either locally imbibition (where the fibres are water-wet) or drainage (where the fibres are hydrophobic). The original model only accommodated primary drainage.

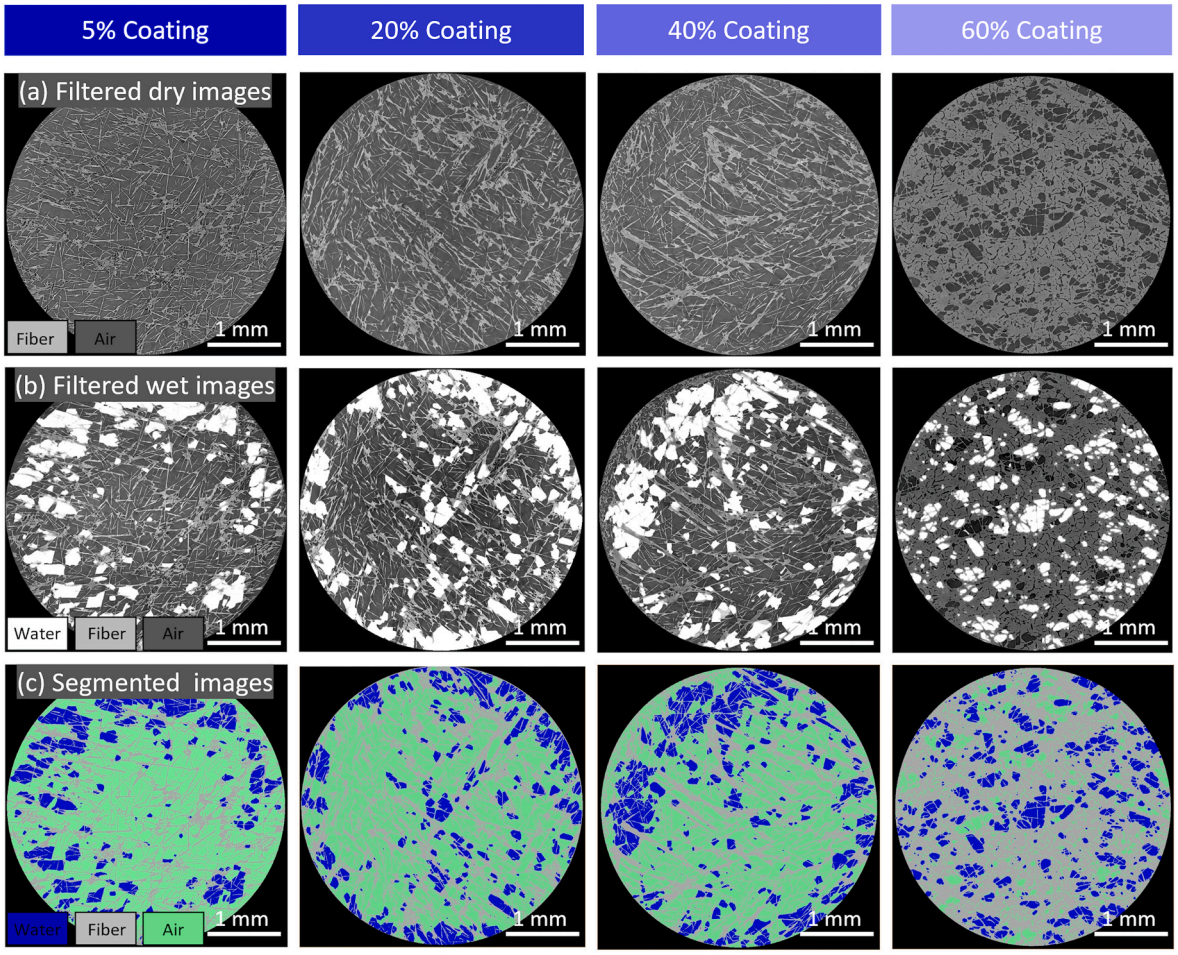

Fig. 2. Greyscale and segmented images for 2D slices of 3D images for different samples (5, 20, 40, and 60% PTFE). (a) filtered dry images that contain air and fibres; (b) Filtered wet images that contain air, brine and fibres; and (c) segmented images that contain air, brine, and fibres.

We modified the network model to include primary imbibition of water into the pore and throat elements. Since this is a primary process, we did not include the presence of wetting layers; these are only found during secondary imbibition, where water is initially present in the pore space. The entry capillary pressure for pore and throat elements was modified. If $0^\circ \leq \theta \leq 90^\circ$, we have an imbibition process and the entry capillary pressure, derived from energy balance that is defined as follows [49]:

$$P_c = \frac{p}{A}\sigma \cos\theta \tag{2}$$

where p is the perimeter of the cross-section of the pore or throat, A is the cross-sectional area and σ is the gas-water interfacial tension. θ is the advancing gas-water contact angle measured through the water phase.

If $90^\circ < \theta \leq 180^\circ$, the process is drainage and the entry capillary pressure is defined as [48,50]:

$$P_c = \frac{\sigma \cos\theta\left(1+2\sqrt{\pi G}\right)}{r} F_d(\theta, G, \beta) \tag{3}$$

where r is the radius of curvature, F_d is the dimensionless correction factor, β is the corner half angle. F_d is defined as:

$$F_d(\theta, G, \beta) = \frac{1+\sqrt{1+\frac{4GD}{\cos^2\theta}}}{\left(1+2\sqrt{\pi G}\right)} \tag{4}$$

The total flow rate is described by calculating the pressure everywhere, imposing mass conservation at every pore i.

$$\sum_j q_{p,ij} = 0 \tag{5}$$

where q_p is the flow rate between pore i and connected throats. j runs over all the throats connected to pore i.

$$q_{p,ij} = \frac{g_{p,ij}}{L_{ij}}\left(\Phi_{p,i} - \Phi_{p,j}\right) \tag{6}$$

where g_p is the fluid conductance. L is the length between the pore centres. Φ_p is the phase potential. $g_{p,ij}$ is the conductance between two pores i and j that takes the value of the harmonic mean of each individual conductance:

$$\frac{L_{ij}}{g_{p,ij}} = \frac{L_i}{g_{p,i}} + \frac{L_t}{g_{p,t}} + \frac{L_{ij}}{g_{p,j}} \tag{7}$$

where t is the connecting throats. L_i and L_j are the lengths from the pore-throat interface to the pore centre for pores i and j, respectively.

For single phase laminar flow g_p is given analytically by the Hagen-Poiseuille formula,

$$g_p = \kappa \frac{A^2 G}{\mu_p} \tag{8}$$

with κ being 1/2, 3/5 or 0.5623 for circular, equilateral triangles and squares, respectively. In multiphase flow an individual polygonal element might contain both oil and water. In this case, expression for each phase conductance derived empirically from numerical simulations of flow in arbitrarily shaped ducts.

The breakthrough point occurs when the water relative permeability is more than zero (the first point water reaches the outlet), and the corresponding capillary pressure and water saturation are defining the breakthrough point.

We randomly assigned advancing contact angles to pores and throats with a specified mean and a normal distribution truncated to lie within 0-180°. We will consider mixed-wet cases that have a mix of hydrophilic ($\theta < 90^\circ$) and hydrophobic ($\theta > 90^\circ$) pores and throats. This means that locally we will have both drainage and imbibition processes at the pore scale, described by Eqs. (2)–(4).

To compare the experimental and model results we performed a pore occupancy analysis. The method involves using the extracted pore network from the dry scan image as an image analysis tool, based on Foroughi et al. [51,52]. Specifically, the inscribed spheres in each pore and throat identified by the pore network extraction from the dry scans are calculated in the same way as performed before for the pore network model. In an experimental image, to determine which fluid resides in each pore or throat, we spatially registered the images so that the same voxel in each of the images corresponds to the same physical location in the sample. The images containing the inscribed spheres labelled with their corresponding pore number or throat number (as extracted from the dry scan) were then overlaid on each wet image. Based on the fluid phase which fills more than 50% of the inscribed spheres centred in a pore or throat in the micro-CT image, we considered that phase as

Table 1
Information regarding the original samples size and sections used for quantitative analysis from which the networks were extracted.

Parameter (2.05 μm/voxels)	5% PTFE	20% PTFE	40% PTFE	60% PTFE
Voxels of the full image	1800 × 1800 × 151	1798 × 1757 × 168	1873 × 1845 × 155	1849 × 150 × 160
Voxels in the model	1200 × 1200 × 151	1200 × 1200 × 168	1200 × 1200 × 155	1200 × 1200 × 160
Number of pores (–)	14,194	12,830	10,278	17,245
Number of throats (–)	62,443	59,175	47,436	28,382

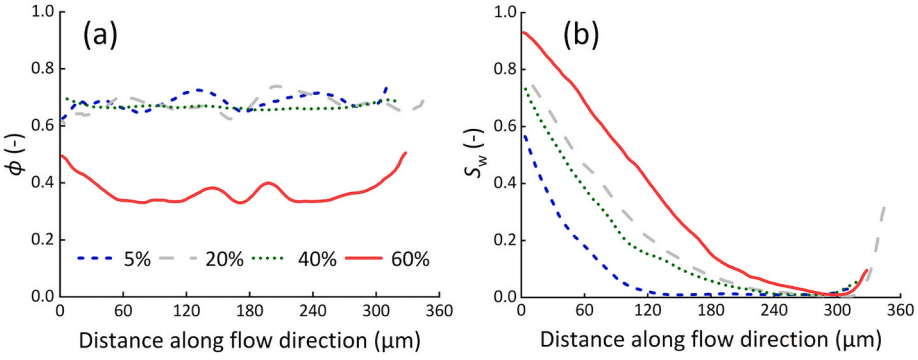

Fig. 3. Porosity and saturation profiles based on segmented images for the different samples (5, 20, 40, and 60% PTFE content). (a) Porosity ϕ, and (b) water saturation S_w.

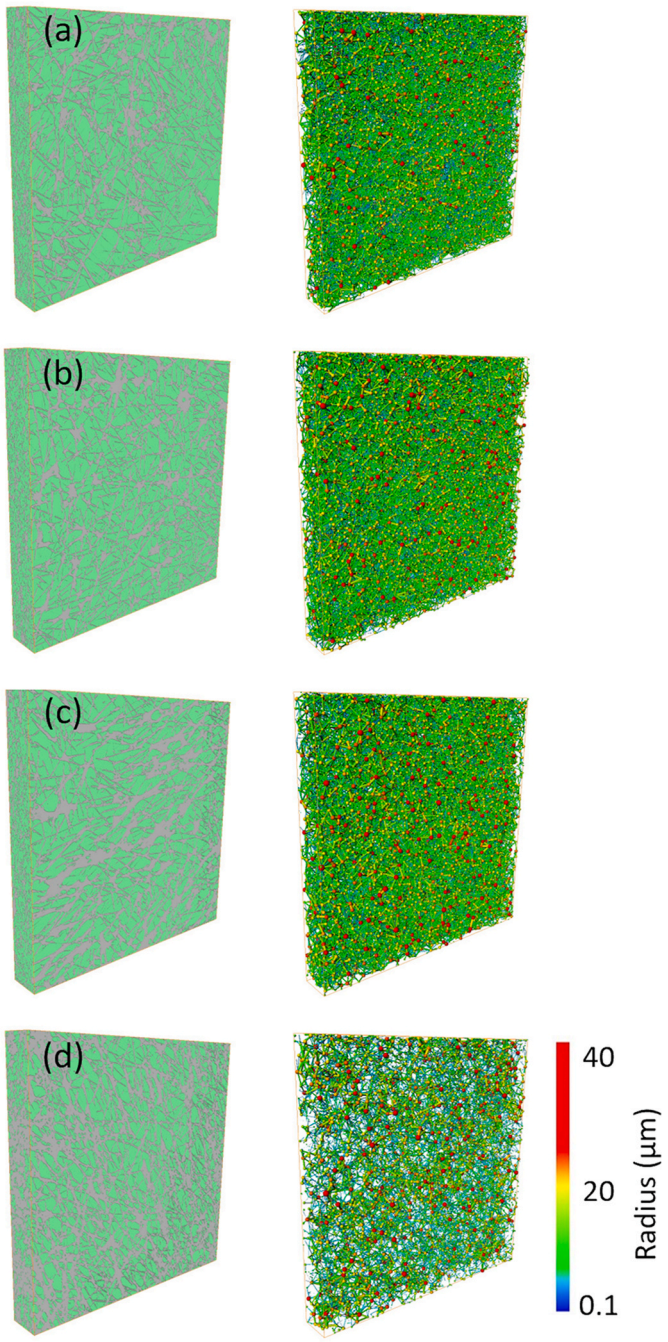

Fig. 4. Visualization of the pore structure for the dry image: (left) greyscale images with fibres in grey and pore space in green; (right) extracted pore networks with warmer colours indicating larger pore/throat radii. PTFE mass fractions of (a) 5%, (b) 20%, (c) 40%, and (d) 60%. (For interpretation of the references to colour in this figure legend, the reader is referred to the Web version of this article.)

occupying the pore or throat. Therefore, this method allows for the accurate quantification of fluid distribution from micro-CT images of GDLs samples obtained from the experiments and in the PNMs.

3. Results and discussion

All the analysis in this paper – the measurements on the images and the network modelling – were based on a cuboidal section of the original cylindrical images. A square cut was taken from the circular cross-section of the images to remove edge effects and voxels that lay outside the GDLs itself. Table 1 lists the sizes of the original images, and the section that was analysed, as well as the number of pores and throats in the extracted network model.

3.1. Measurement of porosity and water saturation

Porosity is a key structural parameter in GDLs, which plays an important role in the transport of water and gas in fuel cells. Fig. 3a shows the slice-average porosity distribution along the flow direction, measured from segmented dry images of GDLs with different PTFE content (5, 20, 40, and 60%). The porosity only shows a significant decrease for the 60% case, consistent with previous analysis [18]. In general, higher porosity is beneficial for liquid water removal from GDLs, as it allows better water transport, which is crucial to preventing flooding in the fuel cell. However, as we will demonstrate later, water transport is also facilitated by the PTFE coating which, despite decreasing porosity, creates a mixed-wet state that allows for

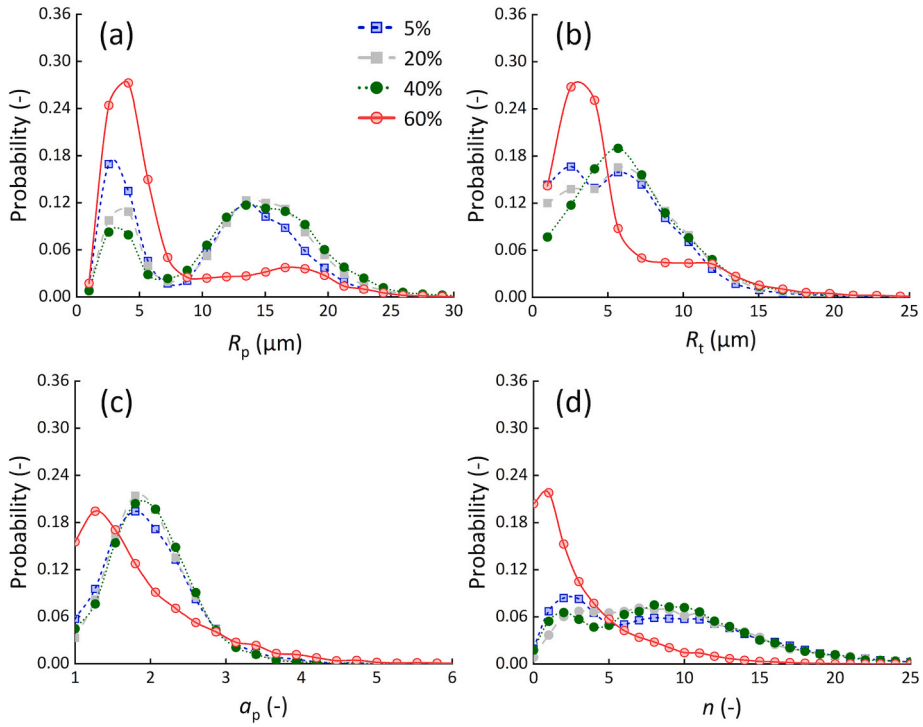

Fig. 5. Statistics and characterization of the pore structure for dry samples (5, 20, 40, and 60% PTFE content). (a) Pore radius distribution (R_p). (b) Throat radius distribution (R_t). (c) Aspect ratio distribution (a_p). (d) Coordination number distribution (n).

simultaneous flow of both water and gas.

Fig. 3b shows the slice-average water saturation measurements from wet images; the results indicate that the water saturation decreases along the flow direction, which is consistent with previous studies [34]. We see that a higher PTFE content leads to higher saturations, as in with previous work which has observed a longer time for breakthrough in hydrophobic compared to hydrophilic GDLs [23,25]. A higher capillary pressure is required to force the water through tighter and more hydrophobic pore spaces with larger PTFE contents, which then allows the water to reach a higher overall saturation. However, the water saturation decreases slightly when the PTFE content increases from 20 to 40%, which indicates the intricate interplay between hydrophobicity, pore structure, and water saturation in GDLs, as discussed later. Moreover, it should be noted that the brine saturation increases slightly near the outlet region as a result of boundary effects in the experiment [25].

In Fig. 4 we visualize the pore structure of GDLs studied by showing the greyscale images and the corresponding pore networks extracted by the method described in Section 2.3. The PTFE coating introduces hydrophobicity throughout the samples which has a profound impact on the two-phase flow characteristics. Fig. 5a shows the pore radius (R_p) distribution of GDLs as the PTFE content increases from 5 to 60%. The results indicate a bimodal pore radius distribution within GDLs, with the first peak occurring at approximately 5 μm and the second peak located at 15 μm. As the PTFE content increases to 60%, size of the first peak increases indicating many smaller pores around 5 μm than in GDLs with a lower PTFE content (5, 20, and 40%), especially in the 40% sample. This result further confirms that a favourable pore structure indeed contributes to a reduction in the breakthrough water saturation observed in Fig. 3b. Fig. 5b shows the throat radius distribution (R_t), which shows trends similar to the pore size distribution. These phenomena can be attributed to the preferential accumulation of PTFE in the pore space where the fibres cross. As the PTFE content increases to 60%, more PTFE begins to attach to the large pores or thicken the carbon fibre.

Fig. 5c and d shows the distribution of the aspect ratio (a_p) and coordination number (n). The average aspect ratio is defined as the ratio of the pore radius to the mean of all connected throat radii [53]. n represents the number of neighbouring throats connected to a pore. Note that in most cases we have very large n, or order 10, which is much higher than encountered in porous rocks which, hitherto, have been the focus of pore network modelling studies [45]. The results demonstrate that a_p and n are similar for the low PTFE contents (5, 20, and 40% coating). However, as the PTFE content increases to 60% both a_p and n decrease significantly.

The impact of PTFE content on the relationship between aspect ratio and pore and throat size is further confirmed by the heat maps in the Supplementary Material Fig. S1. In general, larger pores and throats are associated with larger aspect ratios and coordination numbers. However, for the smaller elements some large values of aspect ratio are seen and this effect is most marked for the 60% sample.

3.2. Breakthrough capillary pressure and water saturation

Capillary-driven flow arises from the pressure difference between the liquid and gas phases. Although the gas pressure remains approximately constant in the fuel cell, the water pressure builds up at the PEM and CL interfaces, acting as the primary driving force for water flow at the cathode. Fig. 6 a-d demonstrates the impact of wettability on breakthrough capillary pressure. Here pore network model predictions for the breakthrough capillary pressure as a function of advancing contact angle distribution with mean values 110°, 120° and 130° and standard deviations up to 15° are shown for mixed wettability GDLs with increasing PTFE content (5, 20, 40, and 60%) and compared with the experimental breakthrough pressure from Shojaei et al. [25]. The shaded regions in the figures represent the standard deviation estimated for different random seeds to assign contact angle in the network model.

As expected, the capillary pressure decreases (becomes more negative) as the contact angle is increased. Above 90° we have hydrophobic conditions, on average, and a positive pressure in the water (defined as a negative capillary pressure) is necessary for water to span the system. The capillary pressure is less negative as the standard deviation of capillary pressure increases. The pore space has a large coordination

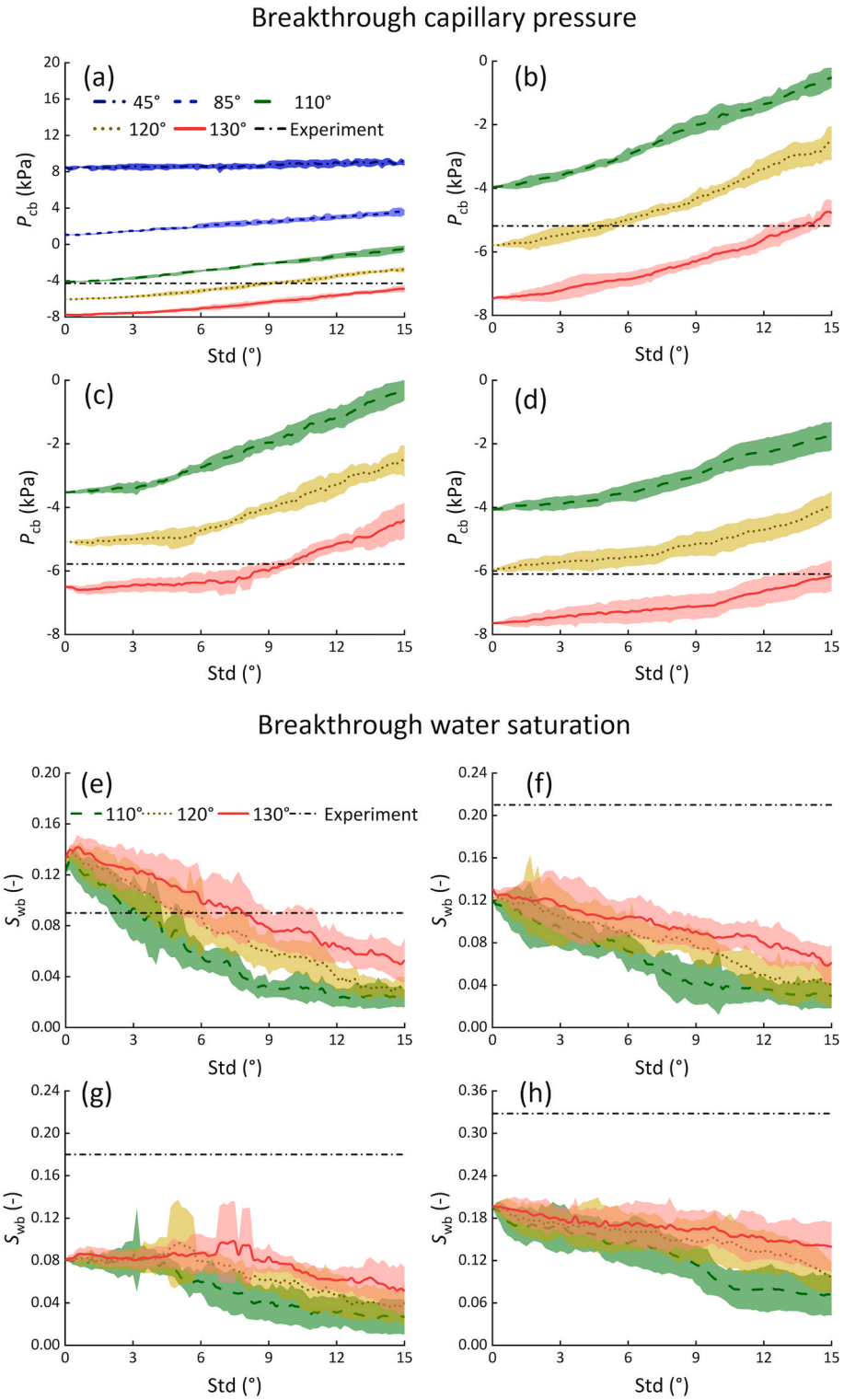

Fig. 6. The sensitivity of breakthrough capillary pressure and water saturation to the advancing contact angle distribution for GDLs with different mass fractions of PTFE: 5% (a),(e); 20% (b),(f); 40% (c),(g); and 60% (d),(h). The shaded areas indicate the standard deviation, resulting from different random seeds to assign contact angle in the network model. Capillary pressure is defined as the difference between the air pressure and water pressure: a negative value indicates that water is at a higher pressure than the air.

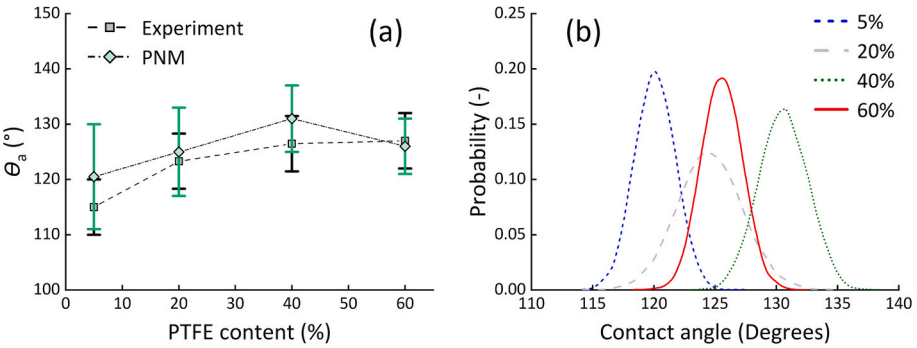

Fig. 7. The PNM predictions of the contact angle and the experimental measurements. (a) Mean advancing contact angle, and (b) contact angle distribution. The advancing contact angles in the experiment were measured directly on the surface of the GDLs [25]. The black error bars show the standard deviation from three independent measurements. The green error bars show the standard deviation of the contact angle distribution in the PNM simulations, see the Appendix. (For interpretation of the references to colour in this figure legend, the reader is referred to the Web version of this article.)

number and so with a wide range of contact angle it is possible for the water to progress through those pores and throats that are less hydrophobic, leading to a lower pressure build-up necessary for water to pass through the pore space.

From Fig. 6a–d it is seen that increasing the PTFE content from 5 to 40% does not increase the breakthrough pressure for the same contact angle distribution. This observation can be explained by the fact that at a lower PTFE content, water flows through the larger pore spaces with lower threshold capillary pressures, for which the pore and throat size distributions are similar, see Fig. 5. The breakthrough capillary pressure increases to maximum negative values of −8 kPa as the contact angle increases, which is consistent with experimental and simulation results [25,26,54]. Specifically, we are able to match the experimentally-measured breakthrough pressure with an appropriate contact angle distribution in all cases.

The breakthrough pressure is negative for all mixed-wet GDLs and this is a direct consequence of enhanced hydrophobicity. To further understand the impact of wettability on the breakthrough capillary pressure we performed additional simulations for the GDL with 5% coating that was conditioned in the model to be water-wet (hydrophilic) with advancing contact angles of 45° and 85° with standard deviation of up to 15°. In Fig. 6a model predictions show positive breakthrough pressures with a maximum of 8 kPa.

Fig. 6e–h shows model predictions for the breakthrough water saturation for advancing contact angle distributions with mean values 110°, 120° and 130° and standard deviation up to 15° in GDLs with increasing PTFE content. The results demonstrate that as the contact angle increases from 110° to 130°, the breakthrough water saturation also increases. This can be attributed to a decrease in breakthrough capillary pressure, resulting in a more negative value. Consequently, higher pressure builds up for water, allowing more water to push into the pore space. The results are compared to the experimental breakthrough saturation measured by Shojaei et al. [25]. The water breakthrough saturation calculated by the PNM simulation is lower than the experimentally measured saturation, and this discrepancy may be attributed to end effects in the experiments which led to retention of the water near the inlet and outlet – see Fig. 3. Nevertheless, the PNM simulation provides valuable insights into the role of contact angle distribution in water transport through GDLs, and the observed trend of increasing breakthrough water saturation with contact angle is consistent with experimental observations in the sense that the more coated samples show a higher saturation.

3.3. Contact angle analysis

Fig. 7 shows the predicted advancing contact angle using PNM methods. As explained further in the Supplementary Material Fig. S2, we found the largest and smallest average contact angle that could match the measured breakthrough pressure in each case. The average of these limiting values is defined as the mean advancing contact angle: 120.5°, 125.0°, 131.0°, and 126.0° for GDLs with 5, 20, 40, and 60% content, respectively. These values are compared with contact angles that are measured directly on the surface of GDLs [25]. The results show that the predicted mean contact angle can match the experimental data. Moreover, the distribution of contact angles predicted in the simulations is 120.5 ± 27.0°, 125.0 ± 30.0°, 131.0 ± 31.5°, and 126.0 ± 31.5° for GDLs with 5, 20, 40, and 60% content, respectively. This provides confidence that the model is correctly represents the wettability in the experiment.

3.4. Fluid occupancy in pores and throats

Fig. 8 shows the water occupancy in all pores and throats in the experiments and model predictions at water breakthrough in GDLs. The model predictions use the same matched wettability as described in the previous section. Since we predict a lower breakthrough saturation than the experiments, see Fig. 8, the area under the distributions is lower for the simulations than the experiment.

At water breakthrough, we observe that water prefers the larger pores and throats, while the smaller elements remained air-filled. The smaller elements – if coated with PTFE – will have a higher threshold entry pressure for water and hence will not be filled with water up to breakthrough [55]. The large pores have lower entry pressures and so are preferentially filled with water. While overall the tendency to fill the larger elements is seen for both the simulations and experiments, the larger saturation seen in the experiments, Fig. 8, means that there is more filling overall than predicted in the PNM.

4. Conclusions

Understanding the pore structure and wettability of GDLs can help improve the performance and efficiency of fuel cells. We used experimental micro-CT imaging and pore network modelling to characterize the pore space and predict breakthrough capillary pressure and water saturation in GDLs of mixed wettability. The conclusions that can be drawn from the results are as follows:

(1) It is possible to use PNMs, originally designed to study multiphase flow in porous rocks, to study fibrous porous media with higher porosities and coordination numbers. The model was extended to allow both primary drainage and imbibition processes.
(2) The GDLs have a bimodal pore size distribution.
(3) Water preferentially flows through the larger pores and throats, while small pores and throats retain air after breakthrough.
(4) The PNM can accurately predict the advancing contact angles in GDLs to match the experimental data once matched to the measured breakthrough water pressure. The model developed in this work can be used to predict the performance of GDLs under a wide range of conditions, beyond those studied experimentally, to proposed novel designs with optimal performance.

These findings suggest that fuel cell performance can be improved by

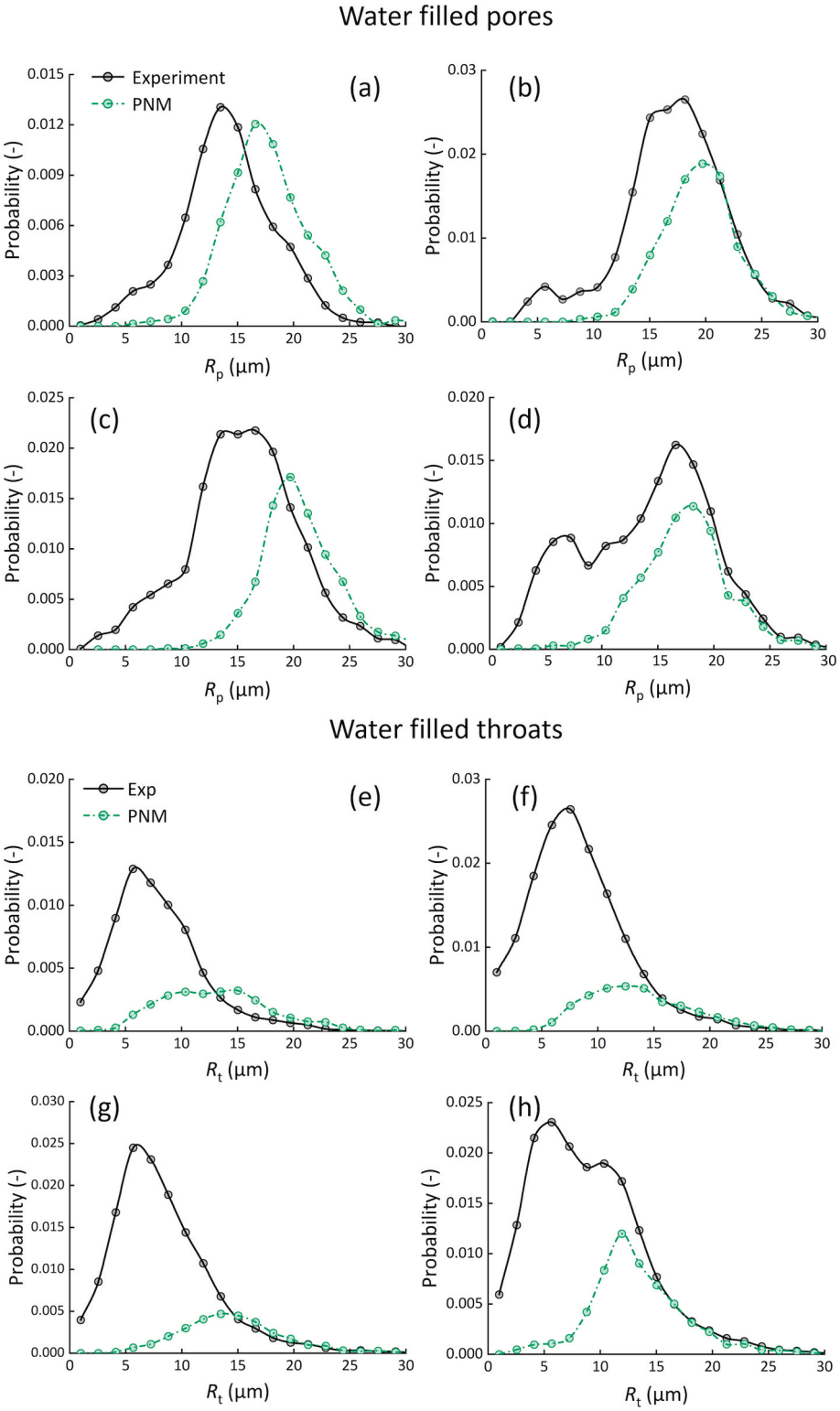

Fig. 8. The occupancy of water-filled pores (a)–(d) and throats (e)–(h) comparing experiment and simulation for PTFE contents of: 5% (a),(e); 20% (b),(f); 40% (c),(g); and 60% (d),(h).

designing the GDLs with an appropriate pore size and wettability distribution.

CRediT authorship contribution statement

Min Li: Conceptualization, Investigation, Formal analysis, Validation, Writing – original draft. **Sajjad Foroughi:** Conceptualization, Investigation, Methodology, Formal analysis, Validation, Writing – review & editing. **Jiafei Zhao:** Conceptualization, Supervision. **Branko Bijeljic:** Conceptualization, Supervision, Writing – review & editing. **Martin J. Blunt:** Conceptualization, Supervision, Writing – review & editing.

Declaration of competing interest

The authors declare that they have no known competing financial interests or personal relationships that could have appeared to influence the work reported in this paper.

Data availability

The image data used in this work can be found on the Digital Rocks Portal: https://www.digitalrocksportal.org/projects/462. The pore-network flow model code and pore occupancy analysis code can be downloaded from the following website link: https://github.com/ImperialCollegeLondon/porescale.

Acknowledgements

All the authors would like to acknowledge Javad Shoajei for help in data provision and the Imperial College Pore-scale Modelling Consortium for funding this work. Min Li would like to thank the China Scholarship Council (Grant 202106060121) for supporting her visit and work at Imperial College London. We thank Dr. Weiwei Fan for providing computer resources for WEKA segmentation, funded by the Henan Provincial Science and Technology Tackling Program (Grant 212102311151).

Appendix A. Supplementary data

Supplementary data to this article can be found online at https://doi.org/10.1016/j.jpowsour.2023.233539.

References

[1] A. Ozden, S. Shahgaldi, X. Li, F. Hamdullahpur, Prog. Energy Combust. Sci. 74 (2019) 50–102.
[2] J. Millichamp, T.J. Mason, T.P. Neville, N. Rajalakshmi, R. Jervis, P.R. Shearing, D. J.L. Brett, J. Power Sources 284 (2015) 305–320.
[3] W.R.W. Daud, R.E. Rosli, E.H. Majlan, S.A.A. Hamid, R. Mohamed, T. Husaini, Renew. Energy 113 (2017) 620–638.
[4] K.N. Kim, J.H. Kang, S.G. Lee, J.H. Nam, C.-J. Kim, J. Power Sources 278 (2015) 703–717.
[5] H. Li, Y. Tang, Z. Wang, Z. Shi, S. Wu, D. Song, J. Zhang, K. Fatih, J. Zhang, H. Wang, Z. Liu, R. Abouatallah, A. Mazza, J. Power Sources 178 (2008) 103–117.
[6] P.K. Sinha, C.-Y. Wang, Chem. Eng. Sci. 63 (2008) 1081–1091.
[7] A. Bazylak, Int. J. Hydrog. Energy 34 (2009) 3845–3857.
[8] J.T. Gostick, M.A. Ioannidis, M.W. Fowler, M.D. Pritzker, J. Power Sources 173 (2007) 277–290.
[9] G. Luo, Y. Ji, C.-Y. Wang, P.K. Sinha, Electrochim. Acta 55 (2010) 5332–5341.
[10] M. Rebai, M. Prat, J. Power Sources 192 (2009) 534–543.
[11] F. Jinuntuya, M. Whiteley, R. Chen, A. Fly, J. Power Sources 378 (2018) 53–65.
[12] D. Zapardiel, P.A. García-Salaberri, J. Power Sources 520 (2022), 230735.
[13] J. Benziger, J. Nehlsen, D. Blackwell, T. Brennan, J. Itescu, J. Membr. Sci. 261 (2005) 98–106.
[14] Z. Fishman, A. Bazylak, J. Electrochem. Soc. 158 (2011) B841–B845.
[15] M. Balakrishnan, P. Shrestha, N. Ge, C. Lee, K.F. Fahy, R. Zeis, V.P. Schulz, B. D. Hatton, A. Bazylak, ACS Appl. Energy Mater. 3 (2020) 2695–2707.
[16] Y.-H. Pai, J.-H. Ke, H.-F. Huang, C.-M. Lee, J.-M. Zen, F.-S. Shieu, J. Power Sources 161 (2006) 275–281.
[17] Z. Fishman, A. Bazylak, J. Electrochem. Soc. 158 (2011) B846–B851.
[18] G.-G. Park, Y.-J. Sohn, T.-H. Yang, Y.-G. Yoon, W.-Y. Lee, C.-S. Kim, J. Power Sources 131 (2004) 182–187.
[19] L. Hao, P. Cheng, J. Power Sources 195 (2010) 3870–3881.
[20] R. Koresawa, Y. Utaka, J. Power Sources 271 (2014) 16–24.
[21] W. Zhang, F. Guo, Y. Zhou, S. Yu, A. Chen, H. Jiang, H. Jiang, C. Li, ACS Appl. Mater. Interfaces 14 (2022) 17578–17584.
[22] A.D. Santamaria, P.K. Das, J.C. MacDonald, A.Z. Weber, J. Electrochem. Soc. 161 (2014) F1184–F1193.
[23] S.H. Tahseen, M. Hoorfar, Transp. Porous Media 105 (2014) 43–55.
[24] Q. Wen, S. Pan, Y. Li, C. Bai, M. Shen, H. Jin, F. Ning, X. Fu, X. Zhou, ACS Energy Lett. 7 (2022) 3900–3909.
[25] M.J. Shojaei, B. Bijeljic, Y. Zhang, M.J. Blunt, ACS Appl. Energy Mater. 5 (2022) 4613–4621.
[26] M. Mortazavi, K. Tajiri, ASME 2013 11th International Conference on Fuel Cell Science, Engineering and Technology collocated with the ASME 2013 Heat Transfer Summer Conference and the ASME 2013 7th International Conference on Energy Sustainability, American Society of Mechanical Engineers Digital Collection, 2013. Paper No: FuelCell2013-18361, V001T01A016.
[27] Z. Niu, Z. Bao, J. Wu, Y. Wang, K. Jiao, Appl. Energy 232 (2018) 443–450.
[28] Z. Niu, K. Jiao, Y. Wang, Q. Du, Y. Yin, Int. J. Energy Res. 42 (2018) 802–816.
[29] N.K. Palakurthi, S. Konangi, A. Kishore, K. Comer, U. Ghia, Eur. J. Mech. B/Fluids 67 (2018) 357–365.
[30] D. Niblett, V. Niasar, S. Holmes, A. Mularczyk, J. Eller, R. Prosser, M. Mamlouk, J. Power Sources 555 (2023), 232383.
[31] L. Zhang, S. Liu, Z. Wang, R. Li, J. Power Sources 554 (2023), 232276.
[32] P. Satjaritanun, S. Hirano, A.D. Shum, I.V. Zenyuk, A.Z. Weber, J.W. Weidner, S. Shimpalee, J. Electrochem. Soc. 165 (2018) F1115–F1126.
[33] L. Guo, L. Chen, R. Zhang, M. Peng, W.-Q. Tao, Energy 253 (2022), 124101.
[34] T. Agaesse, A. Lamibrac, F.N. Büchi, J. Pauchet, M. Prat, J. Power Sources 331 (2016) 462–474.
[35] M.J. Blunt, B. Bijeljic, H. Dong, O. Gharbi, S. Iglauer, P. Mostaghimi, A. Paluszny, C. Pentland, Adv. Water Resour. 51 (2013) 197–216.
[36] D. Wildenschild, A.P. Sheppard, Adv. Water Resour. 51 (2013) 217–246.
[37] J.C. Parker, Rev. Geophys. 27 (1989) 311–328.
[38] A. Alhosani, A. Scanziani, Q. Lin, A.Q. Raeini, B. Bijeljic, M.J. Blunt, Sci. Rep. 10 (2020) 8534.
[39] M.J. Blunt, Phys. Rev. E 106 (2022), 045103.
[40] Y. Zhang, B. Bijeljic, Y. Gao, S. Goodarzi, S. Foroughi, M.J. Blunt, Geophys. Res. Lett. 50 (2023), e2022GL102383.
[41] A. Lamibrac, J. Roth, M. Toulec, F. Marone, M. Stampanoni, F.N. Büchi, J. Electrochem. Soc. 163 (2015) F202–F209.
[42] C.P. Liu, P. Saha, Y. Huang, S. Shimpalee, P. Satjaritanun, I.V. Zenyuk, ACS Appl. Mater. Interfaces 13 (2021) 20002–20013.
[43] A. AlRatrout, M.J. Blunt, B. Bijeljic, Proc. Natl. Acad. Sci. U.S.A. 115 (2018) 8901–8906.
[44] I. Arganda-Carreras, V. Kaynig, C. Rueden, K.W. Eliceiri, J. Schindelin, A. Cardona, H. Sebastian Seung, Bioinformatics 33 (2017) 2424–2426.
[45] H. Dong, M.J. Blunt, Phys. Rev. E 80 (2009), 036307.
[46] A.Q. Raeini, B. Bijeljic, M.J. Blunt, Phys. Rev. E 96 (2017), 013312.
[47] T. Bultreys, Q. Lin, Y. Gao, A.Q. Raeini, A. AlRatrout, B. Bijeljic, M.J. Blunt, Phys. Rev. E 97 (2018), 053104.
[48] P.H. Valvatne, M.J. Blunt, Water Resour. Res. 40 (2004), W07406.
[49] M.J. Blunt, Cambridge University Press, (2017).
[50] P.-E. Oren, S. Bakke, O.J. Arntzen, SPE J. 3 (1998) 324–336.
[51] S. Foroughi, B. Bijeljic, Q. Lin, A.Q. Raeini, M.J. Blunt, Phys. Rev. E 102 (2020), 023302.
[52] S. Foroughi, B. Bijeljic, M.J. Blunt, Transp. Porous Media 138 (2021) 285–308.
[53] Y. Tanino, M.J. Blunt, Water Resour. Res. 48 (2012), W08525.
[54] M. Mortazavi, K. Tajiri, Int. J. Hydrog. Energy 39 (2014) 9409–9419.
[55] J. Dujc, A. Forner-Cuenca, P. Marmet, M. Cochet, R. Vetter, J.O. Schumacher, P. Boillat, J. Electrochem. Energy Convers. Storage 15 (2018), 021001.